

Defect engineering in BaSnO₃ and SrSnO₃ thin films through nanoscale substrate patterning

Received: 6 November 2024

Accepted: 16 September 2025

Published online: 28 October 2025

 Check for updatesSupriya Ghosh¹✉, Fengdeng Liu^{1,2}, Jay Shah¹, Silu Guo¹, Mayank Tanwar¹, Donghwan Kim¹, Sreejith Nair¹, Matthew Neurock¹, Turan Birol¹, Bharat Jalan¹ & K. Andre Mkhoyan¹✉

Creating 1D or 2D extended defects in thin films that propagate throughout the film thickness enables engineering nanoscale materials with anisotropic properties governed by these defects. Performing defect engineering of thin films with location specificity facilitates new nanoscale device architectures that harness the unique properties of these anisotropic extended defects. Here we demonstrate that, by combining Ga focused ion-beam (FIB) exposure and subsequent heat treatment, it is possible to pattern nanoscale structural perturbations on the substrate surface that promote nucleation and propagation of extended defects in thin films epitaxially grown on these substrates. Using SrTiO₃ as a substrate for growing perovskite BaSnO₃ and SrSnO₃ thin films, we demonstrate engineering ultra-high densities of threading 1D dislocations and 2D Ruddlesden-Popper faults with nanometer-level location specificity limited only by the resolution of the patterning Ga ion-beam of the FIB. Given the versatility of this method, it can be applied to different substrates and films, serving as a flexible means of defect-driven material engineering.

Advances in nanotechnology have shown that many materials, when confined to nanoscale dimensions, exhibit unique properties, making them scientifically stimulating and technologically desirable. While research in thin film and nanoparticle synthesis has shown that many of these nanoscale materials can be pushed further into the sub-nm regime, an alternative path for new science and next-generation technology is possible through engineering naturally-occurring defects in them, especially extended defects. These extended defects—line (or 1D, dislocations and disclination, etc.) and planar (or 2D, grain boundaries, stacking faults, etc.)—are particularly promising because they span the entire crystal in one or two directions while remaining atomically abrupt in others¹. Additionally, since they occupy a very small volume fraction of the host crystal ($\leq 10\%$), nanostructures can leverage the properties of both defect and host. Extended defects in perovskite crystals, especially in perovskite oxides (ABO₃), are particularly promising. The structural flexibility of

these crystals allows them to accommodate various types of distortions, including octahedral BO₆ tilts^{2,3}, uniaxial and biaxial strains^{4,5}, orbital ordering^{6,7}, and cation ordering⁸. Compositional complexity of perovskite oxides combined with such high structural flexibility also allows them to host a wide variety of defects, including unique extended defects, such as inclusion of Ruddlesden-Popper (RP) faults and phases^{9–11}, Aurivillius phase¹², new kinds of 1D defects^{13–15} and dislocations with non-conventional cores¹⁶.

Since extended 1D and 2D defects in these crystals are accompanied by local strain and variation in composition, they often exhibit enhanced electrical, catalytic, or electrochemical properties and, in some cases, originate new phenomena^{14–18}. They are particularly well documented for dislocations and RP faults^{16,19,20}. In ceramic oxide films, dislocations can introduce localized conductive channels, as seen in α -Al₂O₃²¹ and AlN films²², in LiNbO₃²³ (along grain boundaries) and cores in La-doped BaSnO₃ films¹⁶. Further, dislocation-driven modulation of

¹Department of Chemical Engineering and Materials Science, University of Minnesota, Twin Cities, Minneapolis, MN, USA. ²Department of Electrical and Computer Engineering, University of Minnesota, Twin Cities, Minneapolis, MN, USA. ✉e-mail: ghosh115@umn.edu; mkhoyan@umn.edu

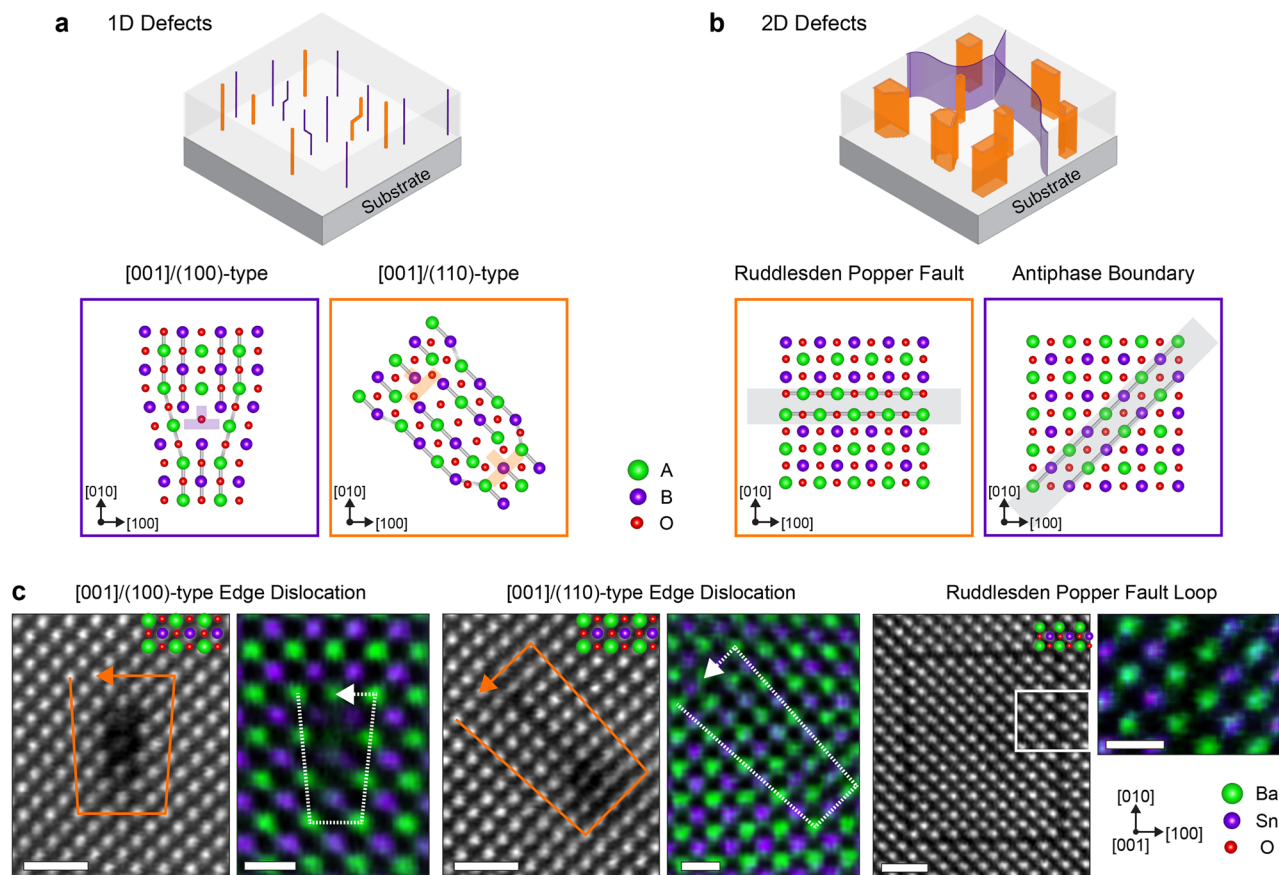


Fig. 1 | Extended defects in perovskite oxides thin films. **a** Illustration of threading 1D line defects in perovskite oxide thin films grown on a substrate along with atomic models of common [001]/(100)-type and [001]/(110)-type edge dislocations with B-terminated cores. The [001]/(110)-type dislocation has a dissociated core with an antiphase boundary in the middle. **b** Illustration of threading 2D planar defects in perovskite oxide thin films. RP fault loops are in orange and grain boundaries are in purple. Atomic models of RP fault and antiphase boundary

are shown in the panels below. **c** HAADF-STEM images of both types of edge dislocations and a RP fault loop from a BaSnO₃ film. The Burgers loops are shown. STEM-EDX maps (the panels on the right) show the Sn-termination of the [001]/(100)-type dislocation core, the antiphase structure of dissociated cores of [001]/(110)-type dislocation and facing BaO planes of the RP fault. Scale bars are 1 nm for the HAADF images and 5 Å for the EDX maps.

piezoelectric and dielectric properties was achieved in BaTiO₃ films²⁴ as well as tuning of superconductivity in plastically deformed SrTiO₃²⁵. Benefits can also be realized with RP faults, such as tunability of the electrocatalytic activity in LaNiO₃ films²⁶. Such property modulations are a result of having different atomic arrangements, localized strain-states, and charged defects, which contribute to the formation of special electronic states in the band structure of the host film.

Nucleation and growth of these defects at high densities in thin films, with nanometer-scale location control, can provide the needed pathway for harnessing their properties and designing new device building blocks for future electronics. The existing techniques of defect management—strain engineering through substrate selection^{26–28}, introduction of buffer layers²⁹, varying composition or temperature during film growth^{30,31}, or through heat or stress treatments^{18,32,33}—are inadequate as they lack location control.

In this work, we present a method for engineering ultra-high-density 1D dislocations and 2D RP faults in perovskite oxide thin films with nanoscale location specificity. The method is based on nanoscale modifications of the substrate surface using ion-beam patterning before film growth. Such surface treatment promotes nucleation of these defects at the film-substrate interface and their propagation through the film. To demonstrate the method, we patterned SrTiO₃ substrates using a Ga ion-beam in a FIB, and subsequently grew thin films of BaSnO₃ and SrSnO₃ using hybrid molecular beam epitaxy (MBE). The analysis of the films using a combination of scanning electron microscopy (SEM) and analytical

aberration-corrected scanning transmission electron microscopy (STEM), shows that ultra-high densities of dislocations and RP faults can be achieved in these films at locations directly above the patterns on the substrate.

Results

In bulk perovskite crystals, the distribution of 1D and 2D defects is relatively isotropic in all directions. However, in thin films grown on a substrate, the direction of crystal growth introduces an anisotropy in their distribution^{1,34}. Due to lattice mismatch between the substrate and the film, the film grows under a substrate-imposed strain, resulting in nucleation of extending defects at the interface, a fraction of which then threads along the film growth direction^{35,36}. The edge dislocations are the most common threading defects in these thin films, followed by 2D RP faults. Among them, edge dislocations of [001]/(100)- and [001]/(110)-types with A- or B-terminated cores^{37,38} are the most prominent (Fig. 1a). RP faults, which consist of two facing AO planes along one of the $\langle 100 \rangle$ directions, in these crystals often appear in the pure form as standalone defects or in the form of loops (either close, or open). In many cases, the RP loops include sections of antiphase boundaries with two facing ABO planes along $\langle 110 \rangle$ directions, as illustrated in Fig. 1b. High-resolution, high angle annular dark-field (HAADF)-STEM images and corresponding elemental energy dispersive X-ray (EDX) maps of two threading dislocations and a RP fault loop from a BaSnO₃ thin film are shown in Fig. 1c, where their characteristic atomic arrangements can be seen.

Nanoscale patterning of SrTiO₃ substrate using an ion-beam

An (001) SrTiO₃ substrate was used here, as it is one of the preferred substrates for growth of both BaSnO₃ and SrSnO₃ films^{39–41}. Ga ion-beam in a dual beam FIB-SEM system was utilized to modify the surfaces of the SrTiO₃ substrates with specific patterns. While a wide variety of different patterns can be made using the FIB system, for simplicity of analysis in this study, all the patterns here were sets of periodically spaced parallel and crossing lines. The characteristics of the lines and the degree of surface modification are directly correlated with the Ga ion-beam dose of the FIB (D_I)^{42,43}. At lower ion-doses, amorphous ridges are created on the substrate surface due to amorphization of the substrate under Ga ion bombardment. At higher ion-doses, in addition to amorphization, trenched channels are created due to partial sputtering of the surface atoms. Figure 2a and b illustrates schematically the differences between low-dose and high-dose patterning with examples. For SrTiO₃ substrates with (001) exposed surfaces, the transition of the patterned line characteristics from low-dose to high-dose regime occurs at about $D_I \simeq 3 \times 10^{17}$ ions/cm²⁴². Three sets of parallel lines patterned on (001) SrTiO₃ substrate, 900 nm apart with varying ion-doses are shown in Fig. 2c. As can be seen, the lines are uniform and the width of the impacted region on the surface widens with an increase of the ion-dose (for more examples, see SI Fig. S1). The structure of these lines was evaluated by HAADF-STEM imaging and STEM-EDX compositional maps obtained from the line cross-sections. One such case for a line patterned with high-dose ions is shown in Fig. 2d, where the trenched channel with the surrounding amorphous region can be seen. More examples of lines made with low- and high-ion-doses are presented in SI Fig. S2. It should be noted that the dimensions of the patterned lines could also be controlled by adjusting Ga ion energy. This is shown in SI Fig. S3.

To ensure that the films of BaSnO₃ and SrSnO₃ grow over the patterned lines with sufficient coherency, recrystallization of the amorphous lines made on the surface of the SrTiO₃ substrate was carried out. It should be noted that a considerable density of imperfections should be preserved in these newly recrystallized lines to nucleate extending 1D and 2D defects. It can be achieved by annealing the patterned substrates at high temperatures, which can be performed either ex-situ, after patterns are made in the FIB, or in-situ in the film growth chamber before growing the thin films. For SrTiO₃ substrates, temperatures between 600 °C < T < 950 °C are found to be optimal, resulting in the creation of the needed recrystallized ridges or channels on the surface (Fig. 2e and f). A set of HAADF-STEM images of the SrTiO₃ substrate with a patterned ridge before and after ex-situ 650 °C heat treatment is shown in Fig. 2g, where the crystallinity of the region is mostly restored, while still containing considerable imperfections. It was observed that as the temperature of heat treatment is increased, higher was the crystallinity of the transformed region with less remaining imperfections. For more details on this amorphous to crystalline transition of the patterned lines on the SrTiO₃ surface, see SI Fig. S4. Further, annealing the patterned substrates created with a lower Ga ion beam energy (8 keV) resulted in similar quality of recrystallized SrTiO₃ substrate (for details, see SI Fig. S5 and S6), which suggests that Ga ion energy could be utilized for further controlling dimensions of the patterned lines and substrate roughness. It should be noted that this patterning method can be applied to many substrates with some modifications of ion-beam parameters⁴².

Growth of BaSnO₃ and SrSnO₃ films on patterned SrTiO₃ substrates

Thin films of BaSnO₃ and SrSnO₃ were grown on these patterned (001) SrTiO₃ substrates by hybrid MBE (Fig. 3a). Before growing the films, the FIB-patterned substrates were in-situ heat-treated inside the MBE chamber at about 900 °C, recrystallizing the amorphous SrTiO₃ around the patterned lines. The 2θ - ω X-ray diffraction (XRD) patterns obtained from these BaSnO₃ and SrSnO₃ films indicate high film quality

and epitaxial relationship between the films and the substrate (Fig. 3b). It should be noted that the BaSnO₃ films are, as expected, in the cubic phase and strain relaxed⁴⁰. The SrSnO₃ films are also as expected for the films grown on (001) SrTiO₃, predominantly in the tetragonal phase and slightly strained (−4.1%)⁴⁴. A combination of SEM surface and STEM cross-section images obtained from the regions of the film grown on non-patterned areas of the substrate confirmed that the films are indeed epitaxially grown on the (001) SrTiO₃ substrate, uniform in thickness, and are of high quality with a nominal concentration of defects. Figure 3c–e and Fig. 3f–h show two such sets of images for BaSnO₃ and SrSnO₃ films, respectively. For more details, see SI Fig. S7 and S8. These observations are consistent with previous reports on BaSnO₃ and SrSnO₃ films grown on (001) SrTiO₃ without any patterning using hybrid MBE^{45,46}.

Next, when SEM images of the surfaces of the films grown over different patterned lines on SrTiO₃ (D_I /separations) were obtained, distinct growth characteristics in these regions, for both BaSnO₃ and SrSnO₃ films, were observed. Atomic-resolution STEM imaging, performed in cross-section and plan-view, allowed to identify the 1D and 2D defects in the patterned regions and quantify their densities.

1D defects in BaSnO₃ films on patterned substrates

Based on the results obtained from BaSnO₃ films grown on non-patterned regions of the substrate (see SI Fig. S7), where fewer defects were observed in the 75 nm-thick BaSnO₃ film, in-depth analysis of threading dislocations in the patterned channels was carried out for the 75 nm thick BaSnO₃ film. A set of SEM images from the film grown directly over patterned lines are shown in Fig. 4a, where cases for two different Ga ion-doses ($D_I = 2.2 \times 10^{16}$ ions/cm² for low-dose and $D_I = 8.3 \times 10^{17}$ ions/cm² for high-dose) and two different spacings between lines (900 nm and 300 nm) are presented. As can be seen, the higher the patterning ion-doses and the smaller the spacing between the lines, the less it resembles the film from the non-patterned region (Fig. 3d). It is particularly visible in void shapes and sizes. For more examples, see SI Fig. S9. The sensitivity of film growth on patterned line size and their proximity is evident, with a more continuous film structure along the channels.

For atomic-level analysis of the BaSnO₃ films grown over the patterned regions, cross-sectional and plan-view STEM imaging were performed. Figure 4b shows a pair of complementary low-magnification HAADF- and low-angle annular dark-field (LAADF)-STEM images obtained in cross-section from the 75 nm-thick BaSnO₃ film grown over a patterned channel in SrTiO₃. The low density of vertical bright lines visible throughout the film in both images are primarily due to threading grain boundaries and dislocations. A strong, bright contrast can be seen at the interface between the film and the substrate in the LAADF image due to strain. This contrast or strain is particularly enhanced and widened in the channel and surrounding areas, which is the result of a more imperfectly recrystallized amorphous channel, discussed earlier (Fig. 2). Atomic-resolution HAADF images of interface inside the channel shows that, while the BaSnO₃ film is grown epitaxially on the SrTiO₃ substrate, considerable interface roughness is still present (Fig. 4c). As indicated earlier, having channels with such surface roughness was intentional to promote nucleation and growth of extended defects. Since BaSnO₃ films prefer hosting threading edge dislocations among extended defects, the film was also analyzed from the plan-view along the film growth direction. For that, a dedicated STEM sample preparation method was developed allowing preparation of electron transparent plan-view, substrate-free, samples of the film from any location on the wafer⁴⁷.

Figure 4d compares two low-magnification HAADF-STEM images of BaSnO₃ films in plan-view obtained from non-patterned and patterned regions. Presence of much smaller columnar grains in the patterned region is evident, which was also observed in cross-section (Fig. 4b). Higher-magnification LAADF images of the film obtained

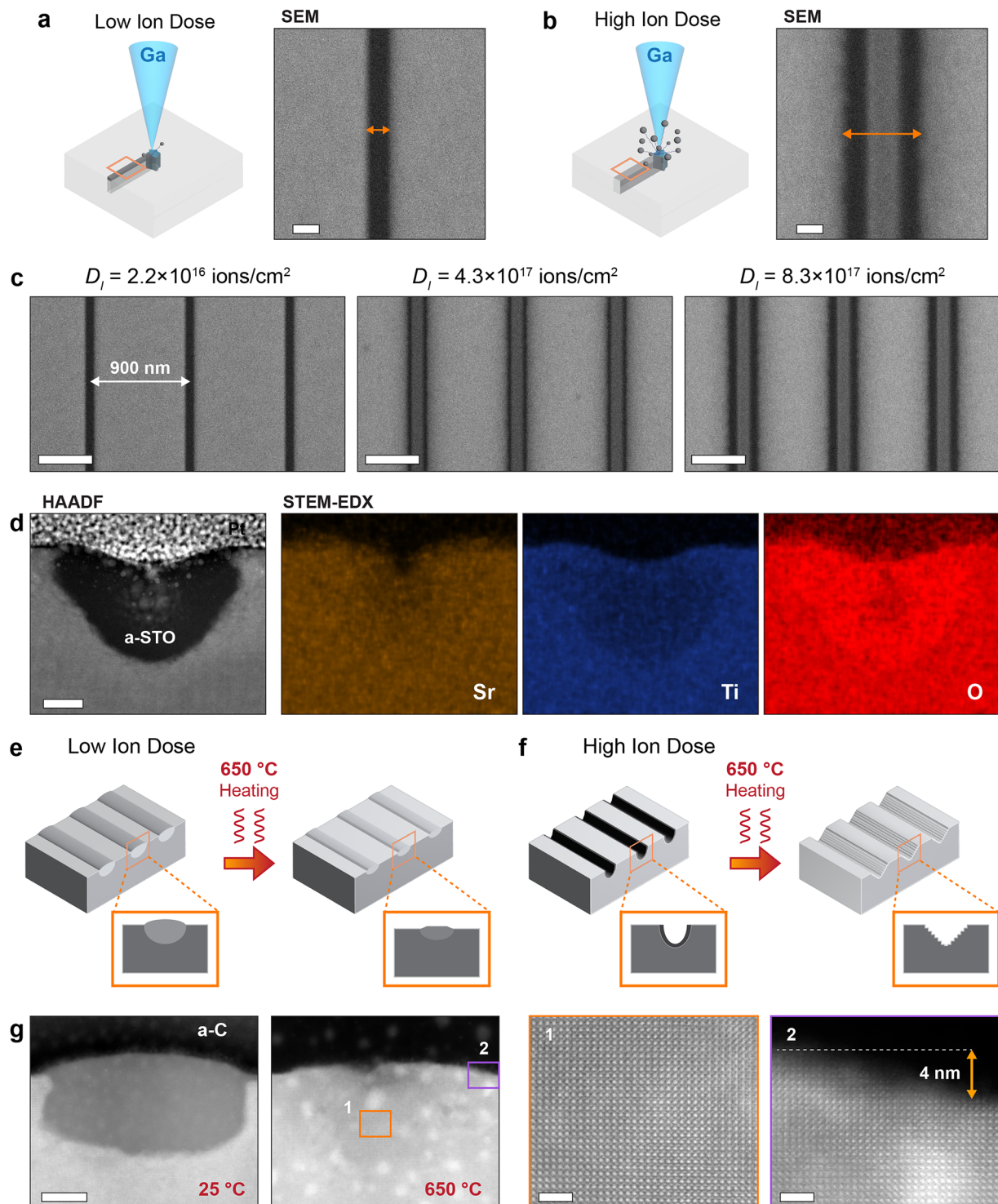


Fig. 2 | Ion-beam patterning of SrTiO₃ substrates. **a, b** Models illustrating patterning of the substrate surface using low-dose and high-dose Ga ions, and corresponding SEM images of such patterned lines on SrTiO₃. Scale bars are 100 nm. **c** SEM images from patterned parallel lines on (001) SrTiO₃ substrate, showing change of structure and increase of line width with increase of ion-dose (D_i). The spacing between pattern lines is 900 nm. Scale bars are 500 nm. **d** Cross-sectional HAADF-STEM image of a line made with $D_i = 8.3 \times 10^{17}$ ions/cm², showing a shallow trenced channel. Dark contrast around the channel is due to amorphized SrTiO₃.

STEM-EDX maps show that the elemental composition of the patterned line is the same as that of the substrate. Scale bar is 20 nm. **e, f** Models illustrating structural modifications of the patterned ridges and channel lines after heat treatment. **g** HAADF-STEM images of patterned ridges on (001) SrTiO₃ substrate, made with $D_i = 4.4 \times 10^{16}$ ions/cm², before and after ex-situ 650 °C heat treatment. Scale bar is 20 nm. Atomic-resolution images, from the boxed areas, show recrystallization of the amorphous patterned line. The brighter dots in the images are Pt particles from the Pt-weld migrated during heating. Scale bars are 2 nm.

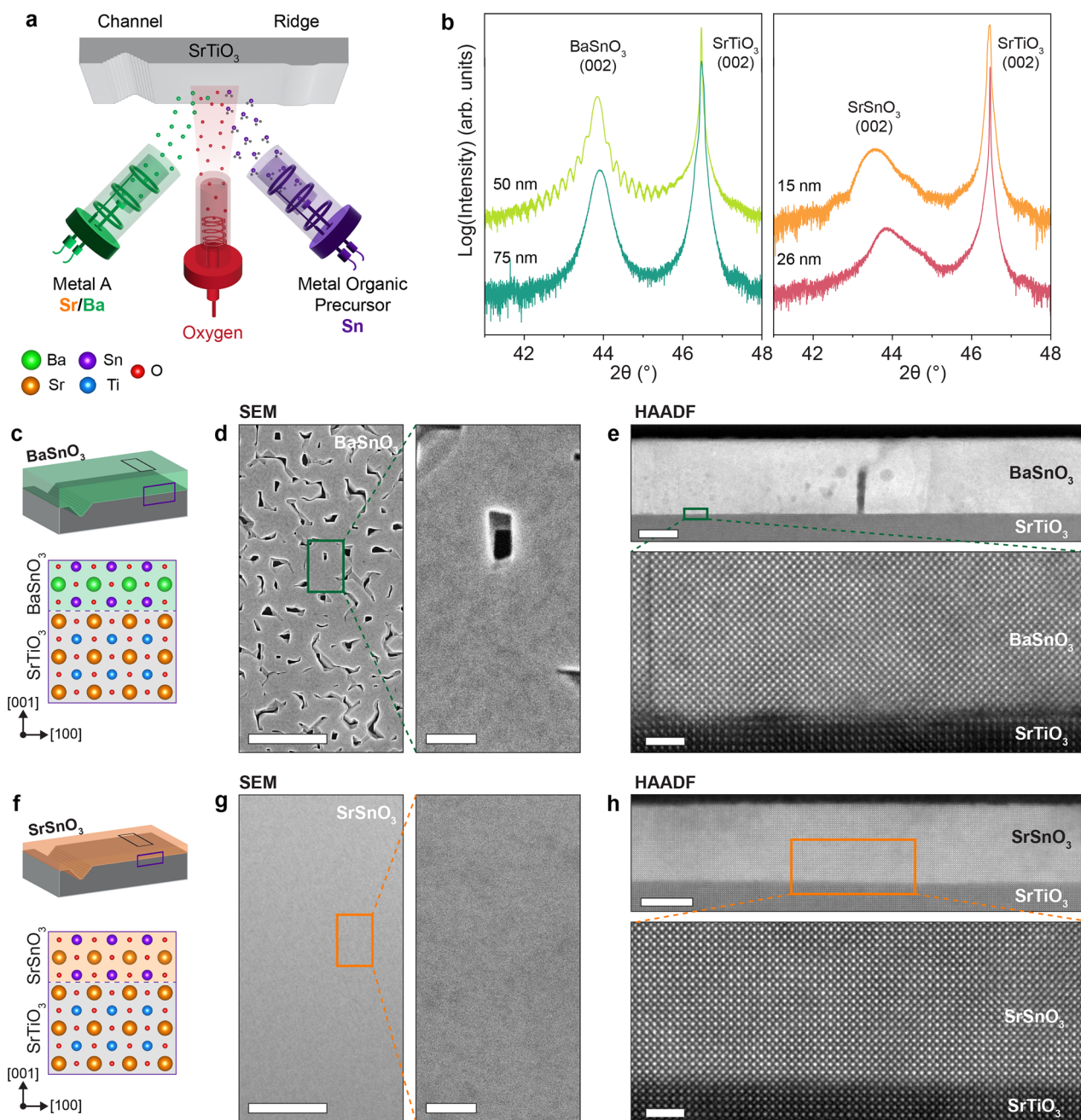


Fig. 3 | Growth of perovskite BaSnO_3 and SrSnO_3 thin films on patterned (001) SrTiO_3 substrates. **a** Schematic illustrating hybrid MBE growth of thin films of BaSnO_3 and SrSnO_3 on the patterned and recrystallized SrTiO_3 substrates. **b** 2θ - ω XRD scans for BaSnO_3 (left) and SrSnO_3 (right) films grown on patterned (001) SrTiO_3 substrates. The film thicknesses are indicated. **c** A model of BaSnO_3 film growth on patterned SrTiO_3 substrate with epitaxial atomic arrangements at the interface between film and substrate. **d** SEM images from a 75 nm-thick BaSnO_3 film from the top surface (dark regions are voids in the film). Scale bars are 1 μm and

100 nm. **e** Low- and high-magnification HAADF-STEM images from BaSnO_3 film in cross-section showing epitaxial growth and uniformity. Scale bars are 50 nm and 2 nm. **f** A model depicting SrSnO_3 film growth on patterned SrTiO_3 substrate with epitaxial atomic arrangements at the interface between SrSnO_3 and SrTiO_3 . **g** SEM images from a 15 nm-thick SrSnO_3 film from the top surface showing uniformity of the film. Scale bars are 1 μm and 100 nm. **h** Low- and high-magnification HAADF-STEM images from SrSnO_3 film in cross-section showing epitaxial growth, uniform 15 nm film thickness, and excellent film quality. Scale bars are 10 nm and 2 nm.

from the same regions shows a dramatic increase in the number of strain-induced bright spots in the film grown over patterned lines (Fig. 4e). The single bright spot is a signature of single-core [001]/(100)-type threading dislocations, and the pair of spots is a signature of [001]/(110)-type dissociated dislocations¹⁶. Atomic-resolution HAADF-STEM images of a few of these dislocations are shown in Fig. 4f. For additional discussion, see SI Fig. S10 and S11.

As discussed earlier, FIB-patterning lines on the surface of the substrate for film growth involves a step of recrystallizing the

amorphous regions surrounding the channels and ridges. As a result, the final widths of the channels, or the ridges, are smaller than that of the original patterned lines. Therefore, for evaluation of threading dislocation densities in the BaSnO_3 film in the patterned region, the area was divided into four sub-regions as follows: 'C' region of the film exactly above the channel after recrystallization of the patterned amorphous line; 'I' impacted region corresponding to the area where the original patterned amorphous line was before recrystallization, 'EI' extended impacted region beyond region 'I' where the film grew

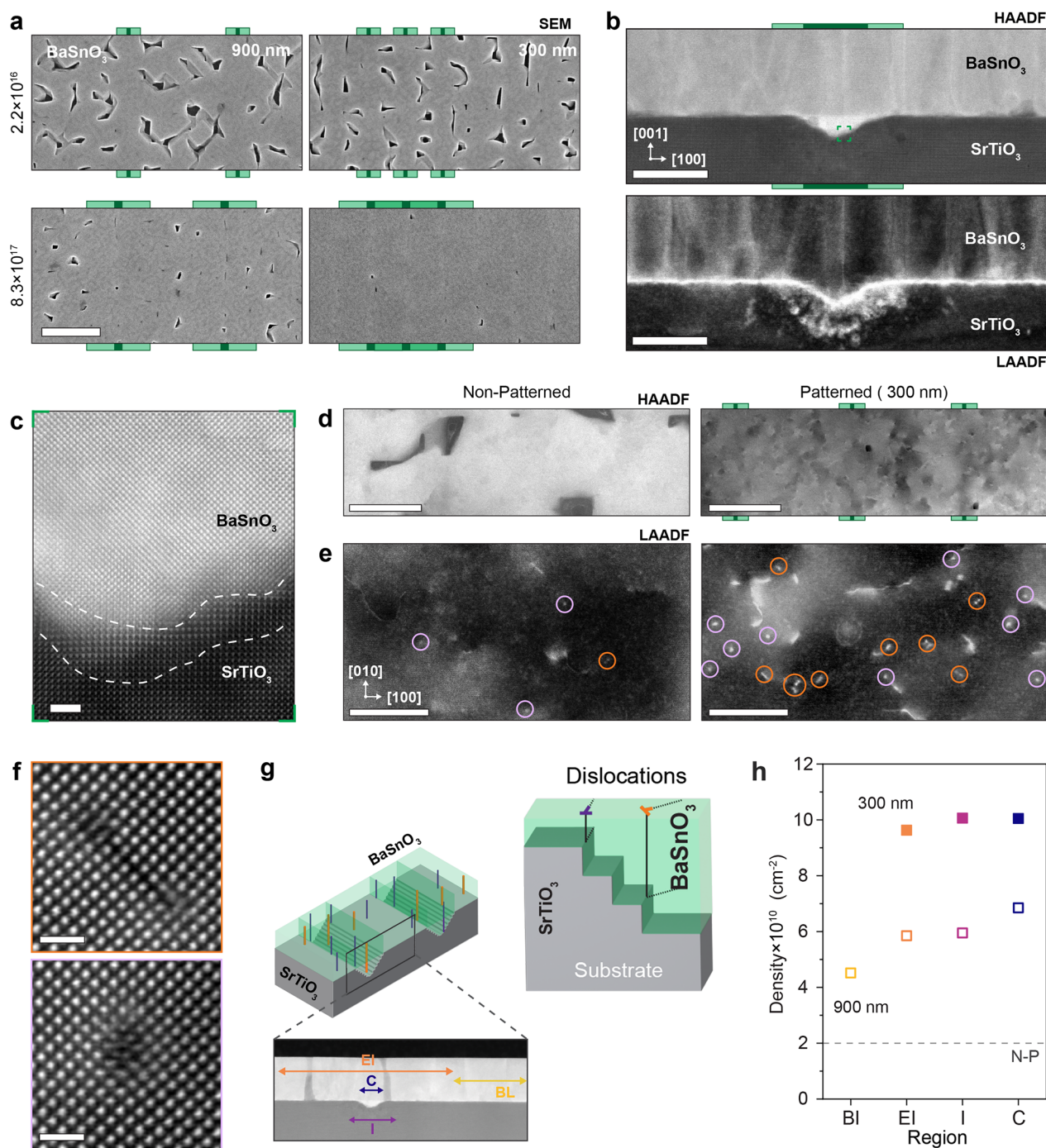


Fig. 4 | Extended defects in BaSnO₃ thin film grown on patterned SrTiO₃. **a** A set of SEM images showing the top surface of the 75 nm-thick BaSnO₃ film grown on the patterned surface of the (001) SrTiO₃ substrate. It includes cases for two different ion-doses, D_1 [ions/cm²], and spacings between patterned lines (900 and 300 nm). Underlying green strips are guides showing the locations of the patterned lines and widths of the channels (dark) and impacted areas (light). Scale bar is 500 nm. **b** A pair of low-magnification HAADF- and LAADF-STEM images of BaSnO₃ film grown over a recrystallized SrTiO₃ channel lines made with $D_1 = 4.3 \times 10^{17}$ ions/cm² ion-beam with 300 nm spacing between them. Scale bars are 50 nm. **c** Atomic-resolution image of the interface between BaSnO₃ film and recrystallized SrTiO₃ substrate from the channel (highlighted with box in (b)) showing epitaxial growth and interface roughness (marked with dashed lines). Scale bar is 2 nm. **d** Plan-view

HAADF images of BaSnO₃ film from non-patterned and patterned regions. Scale bars are 200 nm. **e** Higher-magnification LAADF images from the same regions as in (d). The bright spots are threading dislocations: [001]/(110)-type single core (purple circles) and [001]/(110)-type dissociated cores (orange circles). Scale bars are 50 nm. **f** HAADF-STEM images of both types of dislocations from the patterned region. Scale bars are 1 nm. **g** A model and STEM image illustrating four sub-regions in the film used for dislocation density estimates along with a model illustrating dislocation formation and propagation from the substrate. **h** Evaluated density of dislocations in BaSnO₃ film in different sub-regions indicated in (g). Here regions with 900 nm and 300 nm spacings between the line were considered. The density of dislocations (2×10^{10} cm⁻²) from the non-patterned (N-P) region is marked with dashed line.

differently than in the non-patterned areas, and 'BL' region between the lines beyond 'EI' regions, where film has all resemblance of the non-patterned region. They are shown schematically in Fig. 4g (also, in SI Fig. S9). The widths of the regions 'C' and 'I' are estimated directly from cross-sectional STEM images, and the widths of 'EI' and 'BL' from top-view SEM images. The evaluated 1D dislocation densities from all four regions are summarized in Fig. 4h. Threading dislocation densities approaching 10^{11} cm^{-2} are achieved along the patterned channel, which is $\times 5$ higher compared to the non-patterned bulk regions. Analysis of the relative fractions of these two types of dislocations in patterned and non-patterned areas indicate that, while [001]/(100)-type threading dislocations are the majority of dislocations in both regions, the relative fraction of [001]/(110)-type dislocations increases from 14% in non-patterned regions to 23% in patterned regions. Further, an increase in the density of RP faults was also observed in these patterned regions going from $1 \times 10^5 \text{ cm}^{-1}$ in the reference regions to $2.2 \times 10^5 \text{ cm}^{-1}$.

Comparisons of the dislocation densities from different sub-regions suggests that surface roughness, introduced from recrystallization of the SrTiO₃ substrate, is the likely origin of this dramatic increase. This is further supported by a gradual decrease in the dislocation density moving away from the channel, approaching the reference concentration for larger line separations. Created surface roughness introduces a 3D strain (in-plane and out-of-plane) along the substrate surface for the growing film, and therefore, is more inductive for nucleating these threading defects. It is different from the common 2D biaxial strain due to lattice mismatch between film and substrate^{48,49}.

2D Defects in SrSnO₃ films on patterned substrates

Here again, based on the results obtained from SrSnO₃ films grown on non-patterned regions of the SrTiO₃ substrate (see SI Fig. S8), where less defects were observed in the 15 nm-thick film, in-depth analysis of threading RP faults in the patterned channels were carried out for the 15 nm-thick SrSnO₃ film. Figure 5a shows a set of SEM images obtained from the SrSnO₃ film grown directly on the patterned lines, comparing three different patterns (cases with $D_I = 2.2 \times 10^{16} \text{ ions/cm}^2$ for low-dose, $D_I = 4.3 \times 10^{17} \text{ ions/cm}^2$ for medium-dose, and $D_I = 8.3 \times 10^{17} \text{ ions/cm}^2$ for high-dose Ga ions) and for two different line spacings (900 nm and 90 nm). Since the film is very thin, the pattern lines on the substrate surface are visible in almost all cases, with the channels created at higher ion-doses showing a more pronounced contrast. As can be seen, the patterning results in the formation of some voids in the film near the lines as well as some texture above the channel, both of which are reduced at smaller line spacings. As was the case with the BaSnO₃ film, lower the patterning ion-doses and larger the spacing between the lines are, more it resembles the film from non-patterned region (Fig. 3g). For more cases, see SI Fig. S12.

Two pairs of cross-sectional low- and high-magnification HAADF-STEM images of the same SrSnO₃ film grown on the patterned recrystallized channels, created with a high ion-dose of $D_I = 8.3 \times 10^{17} \text{ ions/cm}^2$ and line spacing of 900 nm line separation and, a medium ion-dose of $D_I = 4.3 \times 10^{17} \text{ ions/cm}^2$ and spacing of 90 nm, are shown in Fig. 5(b) (see also SI Fig. S13). As can be seen, similar to the case of the BaSnO₃ film, despite the presence of considerable substrate surface roughness, the SrSnO₃ film grows epitaxially everywhere, including in the channels. It should be noted here that the depth and the shape of the recrystallized channels are a function of ion-dose⁴². High density of contrast variations visible in the SrSnO₃ in the channels is indicative of a highly defective local structure of the film. Atomic-resolution images of the film obtained from the channels show that the high-density of dark vertical lines visible in the high-magnification images are 2D RP faults propagating through the SrSnO₃ film (Fig. 5c). Differences in the atomic arrangements of different RP faults in this image are due to (i) crystallographic orientation of the faults and (ii) the projection it is being viewed in (for in-depth discussion, see SI Fig. S14).

HAADF-STEM images obtained from the interface between SrSnO₃ and SrTiO₃ inside the recrystallized channels show that the film grows epitaxially on the substrate with a rough surface, (1–3 nm in roughness), and a correlation between the structure of the film and the substrate surface (Fig. 5d). Atomic-resolution images in Fig. 5 show that the nucleation sites of the RP faults in the film coincide with the atomic steps formed at recrystallized SrTiO₃ surface in the channel, as seen in the model in Fig. 5e. It is particularly evident at the slopes of the channels, where more steps are present (for more examples, see SI Fig. S15). Correlation between steps on the substrate and RP faults was also observed in LaNiO₃/LaAlO₃ superlattices⁵⁰. This correlation can be understood through the 3D strain that a rough substrate surface imposes on the growing film. The results of density functional theory (DFT)-based calculations that minimize the surface energies for SrTiO₃ surfaces⁵¹, show that steps on the substrate surface create strain in the in- and out-of-plane directions (see SI Fig. S16). They also show that the higher the slope angle of the surface, the higher are the in- and out-of-plane surface strains imposed on the growing film (for in-depth discussion, see SI Fig. S17). This 3D surface strain, which can be as high as 3 to 6%, in turn forces more nucleation of RP faults. The presence of these surface strains at the film-substrate interface at the patterned sites is readily observed in the LAADF-STEM images (see SI Fig. S17).

The density of these engineered RP faults in the channels was quantified as a function of substrate surface slope angle (Fig. 5f). As seen from the HAADF images, the density of the RP faults is very high and has an identifiable slope dependence. The density of the RP faults in the channels is larger than $2 \times 10^6 \text{ cm}^{-1}$, reaching $4 \times 10^6 \text{ cm}^{-1}$ at the 45° inclined slopes. Such densities are not only $\times 10^3$ higher than those observed in non-patterned regions of the film, but they are close to the theoretical limit of RP fault packing in SrSnO₃. When the lattice constants of SrSnO₃ were calculated using DFT, the results indicated that the maximum density of RP faults that SrSnO₃ can maintain without a large internal stress (i.e., without a significant change in the lattice parameter) is one per 5-unit-cells, or $4.8 \times 10^6 \text{ cm}^{-1}$, beyond which there is a large strain difference between the RP and the bulk perovskite, which would lead to different strain relaxation (for in-depth discussion, see SI Fig. S18). This is also supported by DFT calculations minimizing the energies of the $n=5$ RP phase of Sr₆Sn₅O₁₆ at different ranges of in-plane strain, indicating formation of these phases can be stabilized (see SI Fig. S19) at different strains.

Since such ultra-high density of RP faults can be created in the patterned areas, their effects on the electronic properties of the host SrSnO₃ film were evaluated through DFT calculations. The calculated band structures of bulk SrSnO₃ and SrSnO₃ containing RP faults 5-unit-cells apart are shown in Fig. 6a, b. Examination of the element-specific electronic density-of-states (DOS) from these structures indicates that the majority of the changes occur in the conduction band within 3.5 to 4.5 eV energies above the conduction band minimum. The changes are primarily due to changes in the bonding environment of Sr and O atoms, which is consistent with the presence of RP fault in the structure (for more details, see SI Fig. S18).

For further analysis, using STEM-EELS site-specific DOS of the RP faults were measured and compared with the DOS of bulk SrSnO₃⁵². By measuring the O K-edges (resulting from $1s \rightarrow 2p$ electron excitations) from the RP fault and a pristine region, the differences in the $2p$ -DOS of the conduction bands are captured and identified (Fig. 6c). The increase in the number of states around 4 eV above the conduction band minimum in the RP faults originated from the modified O($2p$)-Sr($3d$) bonds at the fault plane. This increase in DOS in RP faults can be seen in calculated O($2p$) and Sr($3d$) conduction band DOS, also shown in Fig. 6c. These observations suggest that the RP faults, like dislocations, indeed have unique local electronic properties that can be utilized. Because of flattening of the bands at Γ point and removal of some degeneracies due to defect-induced symmetry reduction and changes in local interatomic bonds (Fig. 6b), considerable reduction of

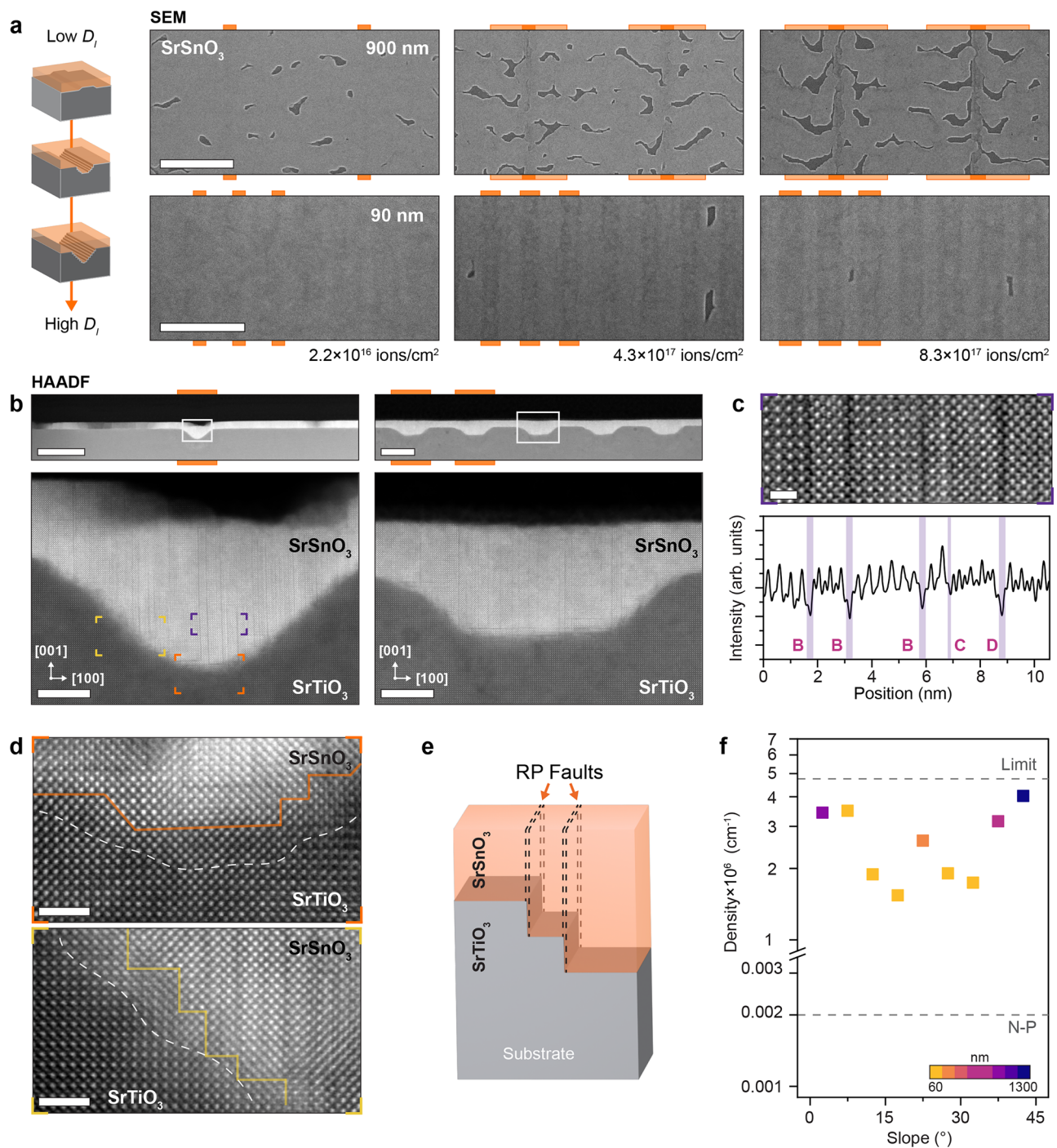


Fig. 5 | Extended defects in SrSnO₃ thin film grown on patterned SrTiO₃. **a** A set of top-view SEM images showing the SrSnO₃ film grown on the patterned surface of the (001) SrTiO₃ substrate with three different D_i and two different line spacings. Underlying orange strips are guides showing the locations and the widths of the patterned lines. Scale bars are 500 nm (top row) and 200 nm (bottom row). **b** Low- and high-magnification HAADF-STEM images of 15 nm-thick SrSnO₃ film grown over recrystallized patterned channels created with ion-doses of $D_i = 8.3 \times 10^{17}$ ions/cm² and 900 nm spacing (left) and $D_i = 4.3 \times 10^{17}$ ions/cm² with 90 nm spacing (right), respectively. Scale bars are 100 and 50 nm (top row) and 10 nm (bottom row). **c** Atomic-resolution image of SrSnO₃ film in the channel, highlighted by the

purple box in **(b)** showing presence of high-density RP faults. HAADF intensity line-scan shown in the panel below with types of RP orientations indicated. The image is low-pass filtered for clarity. Scale bar is 1 nm. **d** HAADF-STEM images from interface between SrSnO₃ film and SrTiO₃ substrate at different locations in the channel (marked in **(b)**) showing epitaxial growth of the film and RP fault nucleation sites. Scale bars are 2 nm. **e** A model illustrating RP fault formation and propagation at the steps of the substrate. **f** Evaluated densities of RP faults as function of channel slope angle. The color map shows the total length over which the density was estimated. The theoretical limit and density of RP faults from the non-patterned (N-P) region (2×10^3 cm⁻¹) in SrSnO₃ are indicated by dash line.

effective masses of charge carriers (for both electrons and holes) as well as changes in local dielectric function are expected.

In summary, localized FIB Ga ion-beam exposure followed by subsequent annealing can produce nanoscale patterns on the surface

of a substrate with built-in roughness, such that thin films grown over the patterned regions will exhibit ultra-high densities of extended defects propagating through the thickness of the film. This is demonstrated by using a common SrTiO₃ wafer as a substrate for

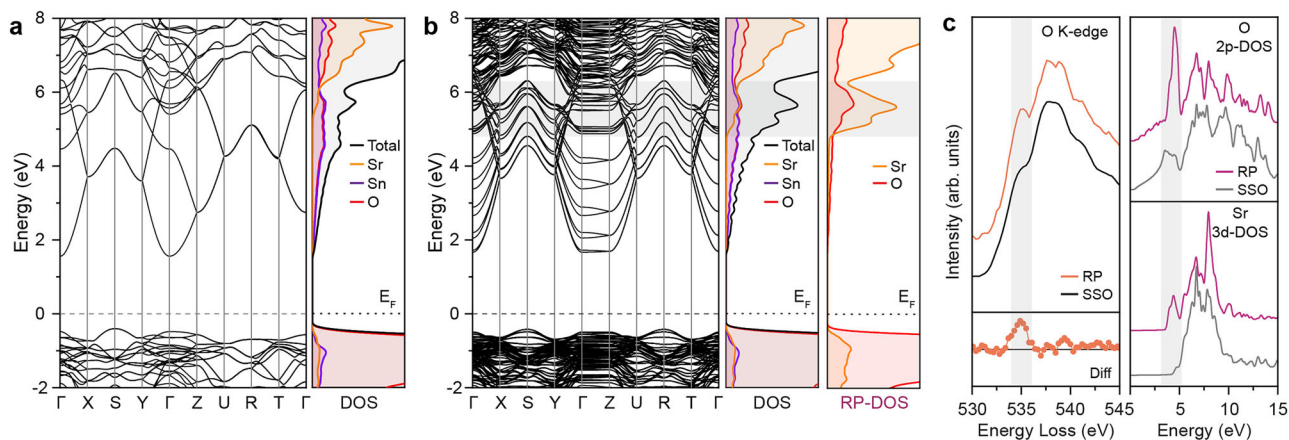


Fig. 6 | Changes in the electronic band structure of the SrSnO₃ film containing RP fault. **a** DFT-calculated electronic band structure (left) and DOS (right) from bulk SrSnO₃ film. **b** Calculated electronic band structure (left) and DOS (right) from the $n = 5$ RP structure based on relaxed atomic structure. The region highlighted in gray shows the region with considerable changes in the conduction band. **c** EELS O

K-edges measured from RP fault and bulk SrSnO₃ film with differences in the fine structure shown below (left). DFT-calculated O $2p$ - (right-top) and Sr $3d$ - (right-bottom) DOS from the RP fault and bulk SrSnO₃. The main differences in EELS spectra and DOS are highlighted in gray matching observations in (b).

growing perovskite oxide BaSnO₃ and SrSnO₃ thin films using hybrid MBE. This approach produces either channels or ridges of desired dimensions on the surface of the substrate with 1–3 nm surface roughness. This roughness, a source of local 3D strain, provides an ultra-high density of defect nucleation sites while still allowing for epitaxial film growth. In the case of BaSnO₃ thin films, locally increased substrate roughness favors the formation of 1D extended defects, such that an order of magnitude higher density of threading dislocations is observed in the patterned SrTiO₃ channels. In the case of SrSnO₃ thin films, patterning-induced roughness favors the formation of RP faults; the density of these 2D defects was found to be three orders of magnitude higher in the patterned channels. These cases show how different types of extended defects can be engineered precisely in specific film regions, with local defect densities approaching the theoretical limit, as was the case for SrSnO₃ films. Since these extended defects have a unique electronic structure, as detailed for dislocations and other line defects in BaSnO₃ in previous studies^{15,16} and for RP faults in SrSnO₃ above, thin films can be produced with different nanoscale regions having different electronic properties. While this approach of engineering extended defects is demonstrated for line patterns, it can be extended to patterns of any shape and size, limited only by the technical capabilities of FIB and other focused ion processing routes. The methods can also be extended to different substrates and films beyond perovskite oxides.

Methods

Substrate patterning

Standard 5 mm (001) SrTiO₃ wafers were patterned using a Ga ion-beam in a FEI Helios G4 dual-beam FIB-SEM system. Prior to loading in the FIB system, the substrates were cleaned in solvents (acetone, isopropyl alcohol, methanol, and distilled water) and air-dried to remove any contamination. The sample chamber in the FIB was plasma cleaned for ~2 hours prior to the wafer loading. The SrTiO₃ wafers were mounted onto screw top SEM holders to prevent contamination, which occurs when conductive carbon tape is used for sample mounting. To prevent ion-beam exposure to the wafer surface, SEM imaging with the secondary electron detector was used to navigate to different positions on the wafer and to monitor patterning. Pattern lines were created on the SrTiO₃ wafer surface with built-in “array” functionality using a 30 keV Ga ion beam with a beam current of 1 pA. Pattern lines were drawn parallel to the (100) or (110) crystallographic directions of SrTiO₃ wafer. The wafers were patterned with ion-doses

ranging from $D_I = 4 \times 10^{14}$ to 8.3×10^{17} ions/cm². Around each patterned region, fiducial markers were made onto the surface to ensure the areas could be located after thin film growth. The patterns were created in the central area of the SrTiO₃ wafer to maximize the uniformity of the films.

Film growth by hybrid MBE

The BaSnO₃ and SrSnO₃ thin films were grown using hybrid MBE^{40,46}. This approach employs conventional effusion cells for La, Ba, and Sr, hexamethylditin (HMDT) as a metal-organic precursor for Sn, and an inductively coupled radio frequency (RF) plasma for oxygen. All films were grown at substrate temperature of 950 °C. The substrates were cleaned in situ with oxygen plasma for 25 min at substrate temperature of 950 °C prior to film deposition. Sr or Ba was sublimed from a titanium crucible separately with its beam equivalent pressure (BEP) measured by a retractable beam flux monitor before growth. The oxygen flow was set to 0.7 sccm to achieve an oxygen background pressure of 5×10^{-6} Torr while applying 250 watts of RF power to the plasma coil. HMDT vapor enters the chamber through a heated gas injector in an effusion cell port that was in direct line-of-site to the substrate. The HMDT bubbler was held at 75 °C to provide sufficient HMDT vapor pressure and the HMDT vapor lines were held at a slightly higher temperature of 85 °C to prevent HMDT condensation in the lines. The injector itself was held at 60 °C. For La: BaSnO₃ 75 nm-thick films, the La cell temperature was fixed at 1220 °C to provide a dopant concentration of 2%.

Characterization of films and defects

The films were characterized using a combination of XRD, SEM, and STEM. A Rigaku SmartLab XE was used for XRD measurements. Film thicknesses were extracted from X-ray reflectivity (XRR). SEM imaging was performed on a Helios G4 dual-beam FIB, using a 15 keV beam and 0.10 nA probe current at a working distance of 3 mm using the backscatter electron detector in the immersion mode. The atomic structures of the films were studied using a combination of LAADF- and HAADF-STEM imaging and the compositional analysis using EDX. Cross-section and plan-view samples for STEM analysis were prepared using the FIB. Here, 30 keV Ga ion beam was used for thinning, followed by 2–5 keV ion beam showers for removing surface damaged layers. Prior to sample preparation, the films were coated with ~50 nm of amorphous carbon in a sputter deposition system to protect the film from damage. STEM imaging and EDX analysis were carried out on an

aberration-corrected FEI Titan G2 60-300 STEM equipped with a CEOS-DCOR probe corrector, a monochromator, and a Super-X EDX detector. The microscope was operated at 200 keV with a probe current of 100–140 pA for imaging and EDX. HAADF and LAADF STEM imaging were performed using detector collection angles of 55–200 mrad and 18–99 mrad, respectively. STEM-EDX maps were collected with drift correction using the Bruker Esprit software. STEM-EELS experiments were carried out using a monochromated STEM beam with a beam current of 40 pA. The energy resolution was 0.13 and 0.4 eV for energy dispersions of 0.01 and 0.1 eV/channel, respectively. All core-level EELS spectra were aligned, background subtracted, and normalized using a post-edge intensity window (600–625 eV) for direct comparison.

Heating experiments of patterned SrTiO₃ substrates in the STEM were carried out using heating chips (from Protochips). The chips are loaded into the Protochips Fusion Select STEM holder and heated to the desired temperature with 2–4 °C/min ramp rate, followed by holding at that temperature for 10–200 mins. Additional imaging was performed after cooling the sample back to room temperature.

DFT calculations of SrSnO₃ RP structures and DOS

First-principles DFT calculations were performed using the projector-augmented wave approach⁵³ as implemented in the Vienna ab initio simulation package (VASP)^{54–56}. The PBEsol exchange correlation functional and PAW potentials were used. A plane wave cutoff energy of 550 eV was used for all calculations. For structure optimization (or relaxation) calculations, residual forces were converged to below 0.001 eV/Å. A 10 × 10 × 10 *Γ*-centered *k*-point mesh was used for SrSnO₃. For Ruddlesden-Poppers, the *k*-point meshes were adjusted to have a similar *k*-point density as for bulk SrSnO₃. Phonon frequencies and eigenvectors were calculated using the frozen phonon approach by constructing dynamical matrices in a basis of symmetry-adapted modes. On this basis, the dynamical matrix is in block diagonal form, where each block corresponds to a single irreducible representation of the space group. The ISOTROPY software suite was used to obtain the symmetry-adapted linear combinations of atomic displacements. For the SrSnO₃, the *R* and *M* point phonon modes of the parent *Pm* $\bar{3}$ *m* (No. 221) structure were calculated. For the Ruddlesden-Poppers Sr_{*n*+1}Sn_{*n*}O_{3*n*+1} (*n* = 1–5), the *X* point phonon modes were considered, since their corresponding atomic displacements are responsible for the oxygen octahedral rotations that are known to dominate the structural phase diagram^{57,58}. The phonon modes with imaginary frequencies were used to determine possible lower-symmetry “distorted” structures. Low-symmetry structures containing either a single or a combination of two normal modes with different symmetries and directions were considered. The Structure Data Converter and Editor tool of the Bilbao Crystallographic Server (BCS) was used to obtain the $\sqrt{2} \times \sqrt{2} \times 2$ supercells from the larger 2 × 2 × 2 supercells, while still capturing the octahedral rotation patterns present in the structures⁵⁹. For the DOS calculations, the Brillouin zone was sampled using a 20 × 20 × 20 *k*-point grid for bulk SrSnO₃. The *k*-point mesh was adjusted to obtain a similar mesh density for the other structures. A 100 meV Gaussian smearing scheme was used for these DOS calculations.

SrTiO₃ structure relaxation

All the SrTiO₃ surface relaxation calculations were carried out using periodic plane-wave DFT methods as implemented in VASP. The Perdew–Burke–Ernzerhof (PBE) functional was used to determine the corrections to the energy due to exchange and correlation effects⁶⁰. D3 dispersion corrections were used to account for the long-range interactions present in the system⁶¹. The structures used in the calculations were constructed from the bulk cubic SrTiO₃ crystal with a lattice constant of *a* = 3.913 Å. For the (100) surface, the bulk SrTiO₃ crystal was cleaved across the (010) plane, and supercells of sizes 4 × 4, 5 × 5, and 6 × 6 were constructed. A vacuum slab was inserted between each

of these surfaces to avoid spurious interactions across the periodic unit cell along the *c*-axis. *Γ*-centered *k*-point mesh of 2 × 2 × 1 was used to sample the Brillouin zone (BZ) for the (010) surface supercells. An energy cut-off value of 400 eV was used. Structural optimizations were carried out in two steps: (1) the wavefunctions were self-consistently optimized to within 10^{−4} eV, and (2) the atomic positions were iteratively optimized until the maximum force was less than 0.08 eV/Å. The wavefunctions were then optimized to within 10^{−6} eV, and the maximum allowable force on each atom was less than 0.05 eV/Å.

Reporting summary

Further information on research design is available in the Nature Portfolio Reporting Summary linked to this article.

Data availability

All the essential data required to evaluate the conclusions in this paper are provided in the article and the Supplementary Information, and are available from the authors upon request.

Code availability

All custom codes used in this study are available from the authors upon request.

References

1. Cai, W. & Nix, W. D. *Imperfections in Crystalline Solids*. (Cambridge University Press, 2016).
2. Kim, T. H. et al. Polar metals by geometric design. *Nature* **533**, 68–72 (2016).
3. Nan, T. et al. Anisotropic spin-orbit torque generation in epitaxial SrIrO₃ by symmetry design. *Proc. Natl. Acad. Sci. USA*. **116**, 16186–16191 (2019).
4. Haeni, J. H. et al. Room-temperature ferroelectricity in strained SrTiO₃. *Nature* **430**, 758–761 (2004).
5. Chaturvedi, V. et al. Room-temperature valence transition in a strain-tuned perovskite oxide. *Nat. Commun.* **13**, 7774 (2022).
6. Yuan, Y. et al. Three-dimensional atomic scale electron density reconstruction of octahedral tilt epitaxy in functional perovskites. *Nat. Commun.* **9**, 5220 (2018).
7. Goodenough, J. B. & Zhou, J.-S. Orbital ordering in orthorhombic perovskites. *J. Mater. Chem.* **17**, 2394–2405 (2007).
8. King, G. & Woodward, P. M. Cation ordering in perovskites. *J. Mater. Chem.* **20**, 5785–5796 (2010).
9. Lee, C. H. et al. Exploiting dimensionality and defect mitigation to create tunable microwave dielectrics. *Nature* **502**, 532–536 (2013).
10. Stone, G. et al. Atomic scale imaging of competing polar states in a Ruddlesden-Popper layered oxide. *Nat. Commun.* **7**, 12572 (2016).
11. Jing, H. M. et al. Formation of Ruddlesden-Popper faults and their effect on the magnetic properties in Pr_{0.5}Sr_{0.5}CoO₃ thin films. *ACS Appl. Mater. Interfaces* **10**, 1428–1433 (2018).
12. Frit, B. & Mercurio, J. P. The crystal chemistry and dielectric properties of the Aurivillius family of complex bismuth oxides with perovskite-like layered structures. *J. Alloy. Compd.* **188**, 27–35 (1992).
13. Maclaren, I. et al. Novel nanorod precipitate formation in neodymium and titanium codoped bismuth ferrite. *Adv. Funct. Mater.* **23**, 683–689 (2013).
14. Jeong, J. S. et al. A new line defect in NdTiO₃ perovskite. *Nano Lett.* **16**, 6816–6822 (2016).
15. Yun, H. et al. Metallic line defect in wide-bandgap transparent perovskite BaSnO₃. *Sci. Adv.* **7**, eabd4449 (2021).
16. Yun, H., Prakash, A., Birol, T., Jalan, B. & Mkhoyan, K. A. Dopant segregation inside and outside dislocation cores in perovskite BaSnO₃ and reconstruction of the local atomic and electronic structures. *Nano Lett.* **21**, 4357–4364 (2021).

17. Armstrong, M. D., Lan, K. W., Guo, Y. & Perry, N. H. Dislocation-mediated conductivity in oxides: progress, challenges, and opportunities. *ACS Nano* **15**, 9211–9221 (2021).
18. Höfling, M. et al. Control of polarization in bulk ferroelectrics by mechanical dislocation imprint. *Science* **372**, 961–964 (2021).
19. De Souza, R. A. Transport properties of dislocations in SrTiO₃ and other perovskites. *Curr. Opin. Solid State Mater. Sci.* **25**, 100923 (2021).
20. Kissel, M. et al. Enhanced photoconductivity at dislocations in SrTiO₃. *Adv. Mater.* **34**, 2203032 (2022).
21. Nakamura, A. et al. Conducting nanowires in insulating ceramics. *Nat. Mater.* **2**, 453–456 (2003).
22. Tokumoto, Y. et al. Fabrication of electrically conductive nanowires using high-density dislocations in AlN thin films. *J. Appl. Phys.* **106**, 124307 (2009).
23. Furushima, Y. et al. Dislocation structures and electrical conduction properties of low angle tilt grain boundaries in LiNbO₃. *J. Appl. Phys.* **120**, 142107 (2016).
24. Zhuo, F. et al. Dislocation density-mediated functionality in single-crystal BaTiO₃. *Adv. Sci.* **11**, 2403550 (2024).
25. Hameed, S. et al. Enhanced superconductivity and ferroelectric quantum criticality in plastically deformed strontium titanate. *Nat. Mater.* **21**, 54–61 (2022).
26. Bak, J. et al. Effect of lattice strain on the formation of Ruddlesden-Popper faults in heteroepitaxial LaNiO₃ for oxygen evolution electrocatalysis. *J. Phys. Chem. Lett.* **11**, 7253–7260 (2020).
27. Ferenc Segedin, D. et al. Limits to the strain engineering of layered square-planar nickelate thin films. *Nat. Commun.* **14**, 1468 (2023).
28. Qi, H. et al. Formation mechanism of Ruddlesden-Popper faults in compressive-strained ABO₃ perovskite superlattices. *Nanoscale* **13**, 20663–20669 (2021).
29. Wang, W. Y. et al. Atomic mapping of Ruddlesden-Popper faults in transparent conducting BaSnO₃-based thin films. *Sci. Rep.* **5**, 16097 (2015).
30. Brooks, C. M. et al. Tuning thermal conductivity in homoepitaxial SrTiO₃ films via defects. *Appl. Phys. Lett.* **107**, 051902 (2015).
31. Mun, H. et al. Large effects of dislocations on high mobility of epitaxial perovskite Ba_{0.96}La_{0.04}SnO₃ films. *Appl. Phys. Lett.* **102**, 0–4 (2013).
32. Fang, X. Mechanical tailoring of dislocations in ceramics at room temperature: A perspective. *J. Am. Ceram. Soc.* **107**, 1425–1447 (2024).
33. Okafor, C. et al. Mechanical tailoring of dislocation densities in SrTiO₃ at room temperature. *J. Am. Ceram. Soc.* **105**, 2399–2402 (2022).
34. Anderson, P. M., Hirth, J. P. & Lothe, J. *Theory of Dislocations*. (Cambridge University Press, 2017).
35. Hu, S. M. Misfit dislocations and critical thickness of heteroepitaxy. *J. Appl. Phys.* **69**, 7901–7903 (1991).
36. Matthews, J. W. & Blakeslee, A. E. Defects in epitaxial multilayers: I. Misfit dislocations. *J. Cryst. Growth* **27**, 118–125 (1974).
37. Zhang, Z., Sigle, W., Kurtz, W. & Rühle, M. Electronic and atomic structure of a dissociated dislocation in SrTiO₃. *Phys. Rev. B - Condens. Matter Mater. Phys.* **66**, 1–7 (2002).
38. Zhang, Z., Sigle, W. & Rühle, M. Atomic and electronic characterization of the a[100] dislocation core in SrTiO₃. *Phys. Rev. B* **66**, 214112 (2002).
39. Raghavan, S. et al. High-mobility BaSnO₃ grown by oxide molecular beam epitaxy. *APL Mater.* **4**, 28–33 (2016).
40. Prakash, A. et al. Hybrid molecular beam epitaxy for the growth of stoichiometric BaSnO₃. *J. Vac. Sci. Technol. A Vac., Surf., Film.* **33**, 060608 (2015).
41. Prakash, A. et al. Wide bandgap BaSnO₃ films with room temperature conductivity exceeding 10⁴ S cm⁻¹. *Nat. Commun.* **8**, 15167 (2017).
42. Ghosh, S. & Mkhoyan, K. A. Quantifying patterned features on material surfaces created using Ga ion beam in FIB-SEM. *Microsc. Microanal.* **31**, oza001 (2025).
43. Giannuzzi, L. A., Prenitzer, B. I. & Kempshall, B. W. Ion - Solid Interactions. in *Introduction to Focused Ion Beams: Instrumentation, Theory, Techniques and Practice* (eds. Giannuzzi, L. A. & Stevie, F. A.) 13–52 (Springer, 2005).
44. Prakash, A. et al. Self-assembled periodic nanostructures using martensitic phase transformations. *Nano Lett.* **21**, 1246–1252 (2021).
45. Prakash, A. et al. Separating electrons and donors in BaSnO₃ via band engineering. *Nano Lett.* **19**, 8920–8927 (2019).
46. Prakash, A. et al. Adsorption-controlled growth and the influence of stoichiometry on electronic transport in hybrid molecular beam epitaxy-grown BaSnO₃ films. *J. Mater. Chem. C* **5**, 5730–5736 (2017).
47. Ghosh, S. et al. Ultramicroscopy Site-specific plan-view (S) TEM sample preparation from thin films using a. *Ultramicroscopy* **270**, 114104 (2025).
48. Jain, S. C., Harker, A. H. & Cowley, R. A. Misfit strain and misfit dislocations in lattice mismatched epitaxial layers and other systems. *Philos. Mag. A Phys. Condens. Matter, Struct. Defects Mech. Prop.* **75**, 1461–1515 (1997).
49. Sando, D. Strain and orientation engineering in ABO₃ perovskite oxide thin films. *J. Phys. Condens. Matter* **34**, 153001 (2022).
50. Detempe, E. et al. Ruddlesden-Popper faults in LaNiO₃/LaAlO₃ superlattices. *J. Appl. Phys.* **112**, 13509 (2012).
51. Heifets, E., Eglitis, R. I., Kotomin, E. A., Maier, J. & Borstel, G. First-principles calculations for SrTiO₃ (100) surface structure. *Surf. Sci.* **513**, 211–220 (2002).
52. Moreira, E. et al. Structural, optoelectronic, infrared and Raman spectra of orthorhombic SrSnO₃ from DFT calculations. *J. Solid State Chem.* **184**, 921–928 (2011).
53. Blöchl, P. E. Projector augmented-wave method. *Phys. Rev. B* **50**, 17953–17979 (1994).
54. Kresse, G. & Hafner, J. Ab initio molecular dynamics for liquid metals. *Phys. Rev. B* **47**, 558–561 (1993).
55. Kresse, G. & Furthmüller, J. Efficiency of ab-initio total energy calculations for metals and semiconductors using a plane-wave basis set. *Comput. Mater. Sci.* **6**, 15–50 (1996).
56. Kresse, G. & Furthmüller, J. Efficient iterative schemes for ab initio total-energy calculations using a plane-wave basis set. *Phys. Rev. B* **54**, 11169–11186 (1996).
57. Wang, T. et al. Engineering SrSnO₃ phases and electron mobility at room temperature using epitaxial strain. *ACS Appl. Mater. Interfaces* **10**, 43802–43808 (2018).
58. Yun, H., Gautreau, D., Mkhoyan, K. A. & Biroli, T. Strain effect on the ground-state structure of Sr₂SnO₄ Ruddlesden-Popper oxides. *Phys. Rev. Mater.* **6**, 104608 (2022).
59. Aroyo, M. I. et al. Crystallography online: Bilbao crystallographic server. *Bulg. Chem. Commun.* **43**, 183–197 (2011).
60. Perdew, J. P., Ernzerhof, M. & Burke, K. Rationale for mixing exact exchange with density functional approximations. *J. Chem. Phys.* **105**, 9982–9985 (1996).
61. Grimme, S., Antony, J., Ehrlich, S. & Krieg, H. A consistent and accurate ab initio parametrization of density functional dispersion correction (DFT-D) for the 94 elements H-Pu. *J. Chem. Phys.* **132**, 154104 (2010).

Acknowledgements

This work was supported primarily by the National Science Foundation (NSF) through award No. DMR-2309431, K.A.M., and partially by the University of Minnesota MRSEC under award No. DMR-2011401, K.A.M., B.J., and T.B. Film growth was supported primarily by NSF through award No DMR-2306273 and partly through DMR-2235208, B.J. Film growth was performed using instrumentation funded by AFOSR DURIP awards FA9550-18-1-0294 and FA9550-23-1-0085, B.J. DFT work was partially

supported by the Office of Naval Research Grant N00014-24-1-2082, T.B. The work was partially supported by DOE award No. DE-SC0024710 (MARIE), M.N., B.J., and K.A.M. Parts of this work were carried out in the Characterization Facility, University of Minnesota, which receives partial support from the NSF through the MRSEC and the NNCI (award No. ECCS-2025124) programs. The authors thank Dr Nick Seaton for assistance with the FIB. S.Ghosh acknowledges support from a Doctoral Dissertation Fellowship from the University of Minnesota.

Author contributions

S. Ghosh and K.A.M. conceived the project. S.Ghosh designed the substrate patterning methods and characterization, and SEM and STEM measurements with inputs from K.A.M. F.L. conducted the thin film growth using hybrid MBE and performed XRD characterization, and D.K. and S.N. contributed to substrate heating studies under the supervision of B.J. S.Ghosh and S.Guo carried out the in-situ heating experiments and analyzed the data. RP structures and band structure calculations were performed by J.S. with inputs from T.B. and K.A.M. Substrate surface structure relaxation calculations were performed by M.T. with inputs from S.Ghosh, K.A.M., and M.N. S.Ghosh and K.A.M. prepared the manuscript with contributions from all authors.

Competing interests

The authors declare no competing interests.

Additional information

Supplementary information The online version contains supplementary material available at <https://doi.org/10.1038/s41467-025-64522-8>.

Correspondence and requests for materials should be addressed to Supriya Ghosh or K. Andre Mkhoyan.

Peer review information *Nature Communications* thanks Sung-Yoon Chung, Junwoo Son, and the other anonymous reviewer(s) for their contribution to the peer review of this work. A peer review file is available.

Reprints and permissions information is available at <http://www.nature.com/reprints>

Publisher's note Springer Nature remains neutral with regard to jurisdictional claims in published maps and institutional affiliations.

Open Access This article is licensed under a Creative Commons Attribution-NonCommercial-NoDerivatives 4.0 International License, which permits any non-commercial use, sharing, distribution and reproduction in any medium or format, as long as you give appropriate credit to the original author(s) and the source, provide a link to the Creative Commons licence, and indicate if you modified the licensed material. You do not have permission under this licence to share adapted material derived from this article or parts of it. The images or other third party material in this article are included in the article's Creative Commons licence, unless indicated otherwise in a credit line to the material. If material is not included in the article's Creative Commons licence and your intended use is not permitted by statutory regulation or exceeds the permitted use, you will need to obtain permission directly from the copyright holder. To view a copy of this licence, visit <http://creativecommons.org/licenses/by-nc-nd/4.0/>.

© The Author(s) 2025